Microstructure and mechanical behaviors of $CoFeNiMnTi_xAl_{1-x}$ high entropy alloys

Peng Cui, Yimo Ma, Lijun Zhang, Mengdi Zhang, Jiantao Fan, Wanqing Dong, Pengfei Yu, Gong Li

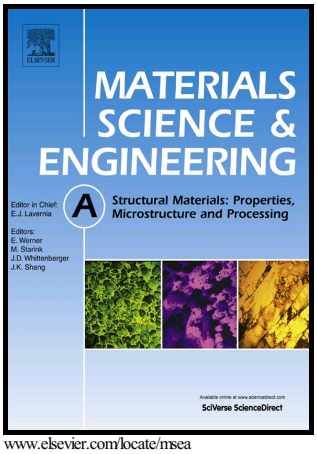

www.elsevier.com/locate/msea

PII: S0921-5093(18)30805-0
DOI: https://doi.org/10.1016/j.msea.2018.06.022
Reference: MSA36577

To appear in: *Materials Science & Engineering A*

Received date: 18 April 2018
Revised date: 4 June 2018
Accepted date: 5 June 2018

Cite this article as: Peng Cui, Yimo Ma, Lijun Zhang, Mengdi Zhang, Jiantao Fan, Wanqing Dong, Pengfei Yu and Gong Li, Microstructure and mechanical behaviors of $CoFeNiMnTi_xAl_{1-x}$ high entropy alloys, *Materials Science & Engineering A,* https://doi.org/10.1016/j.msea.2018.06.022

Microstructure and mechanical behaviors of $CoFeNiMnTi_xAl_{1-x}$ high entropy alloys

Peng Cui, Yimo Ma, Lijun Zhang, Mengdi Zhang, Jiantao Fan, Wanqing Dong, Pengfei Yu, and Gong Li*

State Key Laboratory of Metastable Materials Science and Technology, Yanshan University, Qinhuangdao 066004, China

*Gong Li: E-mail gongli@ysu.edu.cn

Abstract

In this study, the microstructure and mechanical properties of $CoFeNiMnTi_xAl_{1-x}$ (where the molar ratio (x) is 0, 0.1, 0.3, 0.5, 0.8, and 1) high entropy alloys (HEAs) were investigated. The body-centered cubic (BCC) phase, face-centered cubic (FCC) phase, and Laves phase were found in the alloy system. With an increase in the Ti content and a decrease in the Al content, the structure changes of the alloys from BCC to BCC + FCC to BCC + FCC + Laves, and then to Laves + FCC phases. The FCC phase is located at the BCC grain boundary. The $CoFeNiMnTi_{0.5}Al_{0.5}$ HEA with a BCC + FCC duplex phase structure shows the optimal performance of both strength and ductility. The yield strength, fracture strength, and fracture strain can reach 1,052.8 MPa, 2,402.4 MPa, and 20.5%, respectively. The hardness reaches HV518.7. Nanoindentation experiments show that the BCC phase is harder than the FCC phase in the $CoFeNiMnTi_{0.5}Al_{0.5}$ HEA. Furthermore, the deformation behaviors of the FCC phase and BCC phase are studied by measuring the first pop-in behavior.

Key words: High entropy alloys; Microstructures; Mechanical properties; Nanoindentation experiments.

1. Introduction

The convention alloys design procedure is typically based on one or two principal component elements and adding a small number of other elements for performance enhancement. A new type of alloys, high entropy alloys (HEAs), has received important attention recently [1]. These novel alloys with five or more metallic elements in equimolar or near equimolar possess higher mixing entropies, and hence favor the formation of solid-solution phases in simple crystal structures, such as face-centered cubic (FCC), body-centered cubic (BCC), hexagonal closed-pack (HCP) and inhibit the formation of intermetallic compounds [2, 3]. HEAs have been reported to have many excellent properties, such as high strength, great fracture toughness, high malleability, outstanding thermal stability and good corrosion resistance [1-7].

The FCC-structured HEAs have good ductility but poor strength. In the past decade, CoCrFeNi-based and CoCrCuFeNi-based HEAs have been widely studied [2, 8-13]. By adding other elements, numerous new alloys were designed for amending the conflict of strength and ductility. Research indicates that alloys with the hard BCC and soft FCC phases would be likely to balance strength and ductility. Al is considered as a strong BCC phase stabilizer and makes a difference in hardening and strengthening FCC-structured HEAs. Previous studies on the $Al_xCoCrFeNi$ and $Al_xCoCrCuFeNi$ HEAs demonstrated that the structure was transformed from FCC to FCC + BCC with increasing the Al content [14, 15]. Ti with a large atomic radius is also commonly added as a strengthening element [16-18]. The CoFeNiMn HEA is also a single-phase FCC solid-solution alloy [19]. Cr is substituted with Mn so as to further reduce the

cost. In addition, Cu is excluded to avoid the segregation. Zuo *et al.* studied the magnetic performance of CoFeMnNiX (X = Al, Cr, Ga, and Sn) HEAs [20]. However, the mechanical properties of the CoFeNiMn-based HEAs are seldom investigated. Therefore, in this study, a novel series of $CoFeNiMnTi_xAl_{1-x}$ HEAs were prepared. By moderating concentrations of Al and Ti, the two-phase (BCC + FCC) $CoFeNiMnTi_{0.5}Al_{0.5}$ HEA shows the optimal performance of both strength and ductility. The nanoindentation technique has been effectively used for examining the properties of HEAs [21-23], such as the elastic-plastic deformation behavior and the creep characteristics. Few papers have studied the mechanical behavior of individual phases in HEAs by nanoindentation. In the present work, we studied the deformation behaviors of different phases in the $CoFeNiMnTi_{0.5}Al_{0.5}$ HEA.

2. Experimental details

The alloys with nominal compositions of $CoFeNiMnTi_xAl_{1-x}$ [where the molar ratios (x) 0, 0.1, 0.3, 0.5, 0.8, 1, correspond to Ti_0Al_1, $Ti_{0.1}Al_{0.9}$, $Ti_{0.3}Al_{0.7}$, $Ti_{0.5}Al_{0.5}$, $Ti_{0.8}Al_{0.2}$ and Ti_1Al_0, respectively] were fabricated by arc-melting of the constituent elements with purity better than 99.9 weight percent (wt.%) in a Ti-gettered high-purity argon atmosphere. The ingots were flipped over and re-melted at least 5 times to ensure chemical homogeneity. The crystal structures of the alloys were detected by X-ray diffraction (XRD) using a D/MAX-2500/PC diffractometer with the Cu Kα radiation from 20° to 100° of 2θ with 4 degree/min. The working voltage and current are 40 kV and 100 mA, respectively. The microstructures were examined by a scanning electron microscope (SEM, Hitachi S-3600), and the chemical compositions were analyzed by

the SEM energy dispersive spectrometry (EDS). Room temperature compression property tests were carried through on ∅ 3×6 mm samples using an Instron 5982 machine under a strain rate of 5×10^{-4} s^{-1}. Vickers hardness measurement was performed using a hardness tester (HVS-1000) under a load of 300g applied for 10 s, and the average value was obtained of 10 points on each specimen.

The nanoindentation test was carried out, using a Hysitron Triboindenter (TI-900) equipped with the in-situ atomic force microscope (AFM), and with a Berkovich diamond tip at room temperature. The effective tip radius was 450 nm. The sample must be polished to a mirror of 10 nm. The two different phases can be identified through the optical microscope equipped on the Triboindenter. Thermal drift was maintained below 0.05 nm/s for excluding the thermal effect. The nanohardness and elastic modulus on different phases were determined by uploading to the maximum load of 7,000 μN at the loading rate of 1,000 μN s^{-1} with a fixed holding time of 2 s, followed by reducing to zero. The incipient plasticity was examined by measuring the first pop-in behavior in the loading segment of the load-displacement (*P*-*h*) curve under a constant loading rate of 50 μN s^{-1} to 1,000 μN.

3. Results and discussions

3.1 Microstructure characterization

The XRD patterns of the $CoFeNiMnTi_xAl_{1-x}$ HEAs are shown in Fig. 1(a). All the HEAs except the Ti_1Al_0 HEA display a primary BCC solid-solution structure. The detailed scans for the (110) peak of the BCC structure are shown in Fig. 1(b). The peak shifts towards a lower 2-theta peak when the Ti content increases and the Al

content decreases. The lattice parameters of the BCC structure are estimated to be 2.8998 Å, 2.9027 Å, 2.9243 Å, 2.9308 Å, and 2.9393Å from the strongest (110) BCC peak of the Ti_0Al_1, $Ti_{0.1}Al_{0.9}$, $Ti_{0.3}Al_{0.7}$, $Ti_{0.5}Al_{0.5}$, and $Ti_{0.8}Al_{0.2}$ HEAs. Figure 2 shows the lattice parameter difference of the BCC matrix as a function of the Ti content. The lattice parameter difference can be expressed as $(|a - a_0|)/a_0$, where a_0 is the lattice parameter of the BCC structure in the Ti_0Al_1 HEA. With the Ti content increases and the Al content decreases, the lattice parameter of the BCC matrix increases. Ti with a large atomic radius dissolved into the BCC matrix, thus leading to the lattice expansion. In addition, as the Ti contents increased and the Al contents decreased, diffraction peaks of the FCC solid-solution structure appear. The secondary FCC solid-solution phases are present in the $Ti_{0.3}Al_{0.7}$ and the $Ti_{0.5}Al_{0.5}$ HEAs. The XRD pattern of the $Ti_{0.3}Al_{0.7}$ HEA is similar to that of the $Ti_{0.5}Al_{0.5}$ HEA. With regard to the $Ti_{0.8}Al_{0.2}$ HEA, beside the BCC and FCC diffraction peaks, there are weak diffraction peaks of Laves phase. The Laves phase is identified as a Fe_2Ti type with a hexagonal C14 structure. The Fe_2Ti-type Laves phase has been found in $CoCrCuFeNiTi_x$ and $AlCoCrFeNiTi_x$ HEAs [24, 25]. For the Ti_1Al_0 HEA, an FCC + Laves duplex phase structure was observed.

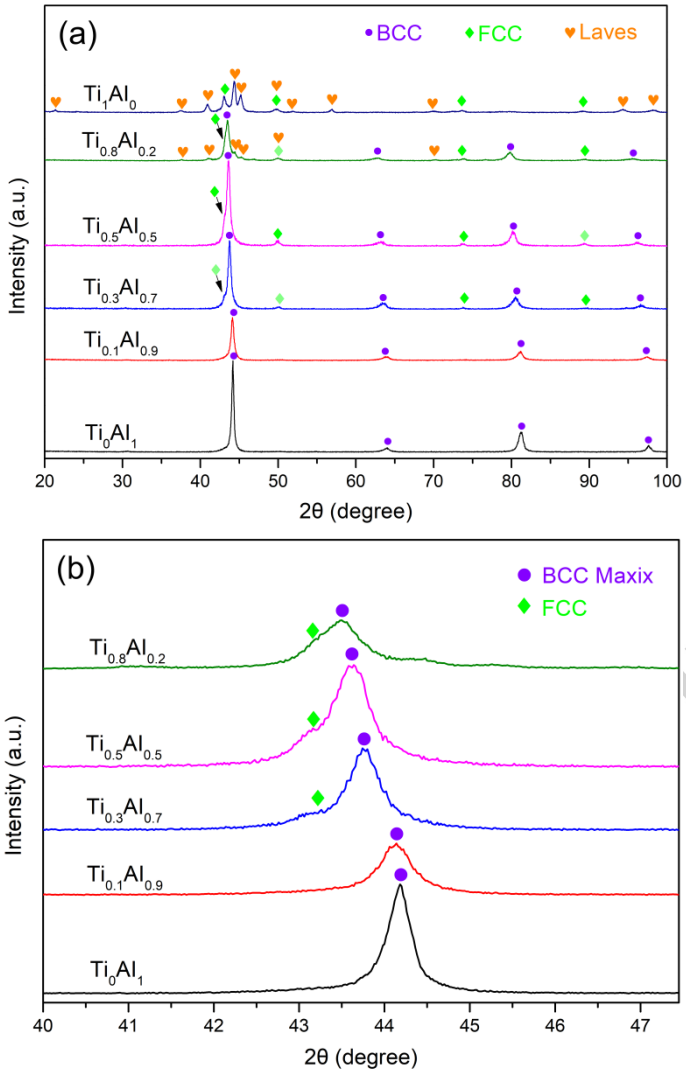

Fig. 1. (a) XRD patterns of the $CoFeNiMnTi_xAl_{1-x}$ (x = 0, 0.1, 0.3, 0.5, 0.8, and 1) HEAs and (b) the detailed scans for the (110) peak of the BCC structure.

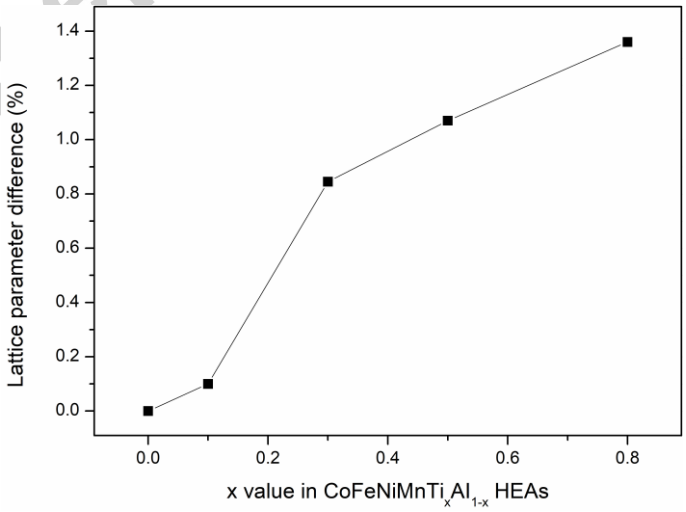

Fig. 2. Lattice parameter difference of the BCC matrix as a function of the Ti content in the

$CoFeNiMnTi_xAl_{1-x}$ (x = 0, 0.1, 0.3, 0.5, and 0.8) HEAs.

The Backscattered images of the $CoFeNiMnTi_xAl_{1-x}$ HEAs are shown in Fig. 3. Table 1 displays the chemical compositions of the alloys. For the Ti_0Al_1 HEA, grain boundaries can be clearly seen. From the Ti_0Al_1 to $Ti_{0.8}Al_{0.2}$ HEAs, the EDS analysis results show that the composition of the BCC solid solution is similar to the nominal composition, indicated by "1". With increasing the Ti content and decreasing the Al content, the SEM results proved that the $Ti_{0.3}Al_{0.7}$ and $Ti_{0.5}Al_{0.5}$ HEAs show an obvious dual-phase structure. The precipitates can be observed along the grain boundary. Combined with the XRD results, the precipitate has an FCC solid-solution structure. The precipitate phase contains more Fe and Mn and fewer Al and Ti, which indicates that Fe and Mn are the FCC-forming elements. The FCC phase is indicated by "2". In fact, the FCC precipitates can be seen along the BCC grain boundaries of the $Ti_{0.1}Al_{0.9}$ HEA and cannot be detected by XRD due to the little content. Ti has high negative enthalpy with other elements (see table 2) [26], which facilitates the formation of the Laves phase. However, the formation of the hexagonal Laves phase may be suppressed upon the addition of Al [18]. For the $Ti_{0.8}Al_{0.2}$ HEA with higher Ti content and lower Al content, the formation of the Laves phase is not completely inhibited. The precipitates are composed of the FCC and Laves phases, indicated by "2" and "3", respectively. The FCC and Laves phases are nearly free of Al. A small amount of Ti dissolves in the FCC phase. The Al-free Ti_1Al_0 HEA has a dual-phase structure, and the precipitates at the grain boundaries are homogeneously distributed rod-shaped particles. Furthermore, the EDS analysis results show that the Laves phase is slightly enriched

(to 22.5-23.2 at.%) with Co, Fe, and Ti, and contain about 15.4-16.1 at.% of both Mn and Ni, which is consistent with previous studies that the Laves phase in HEAs is a multicomponent phase [27-29].

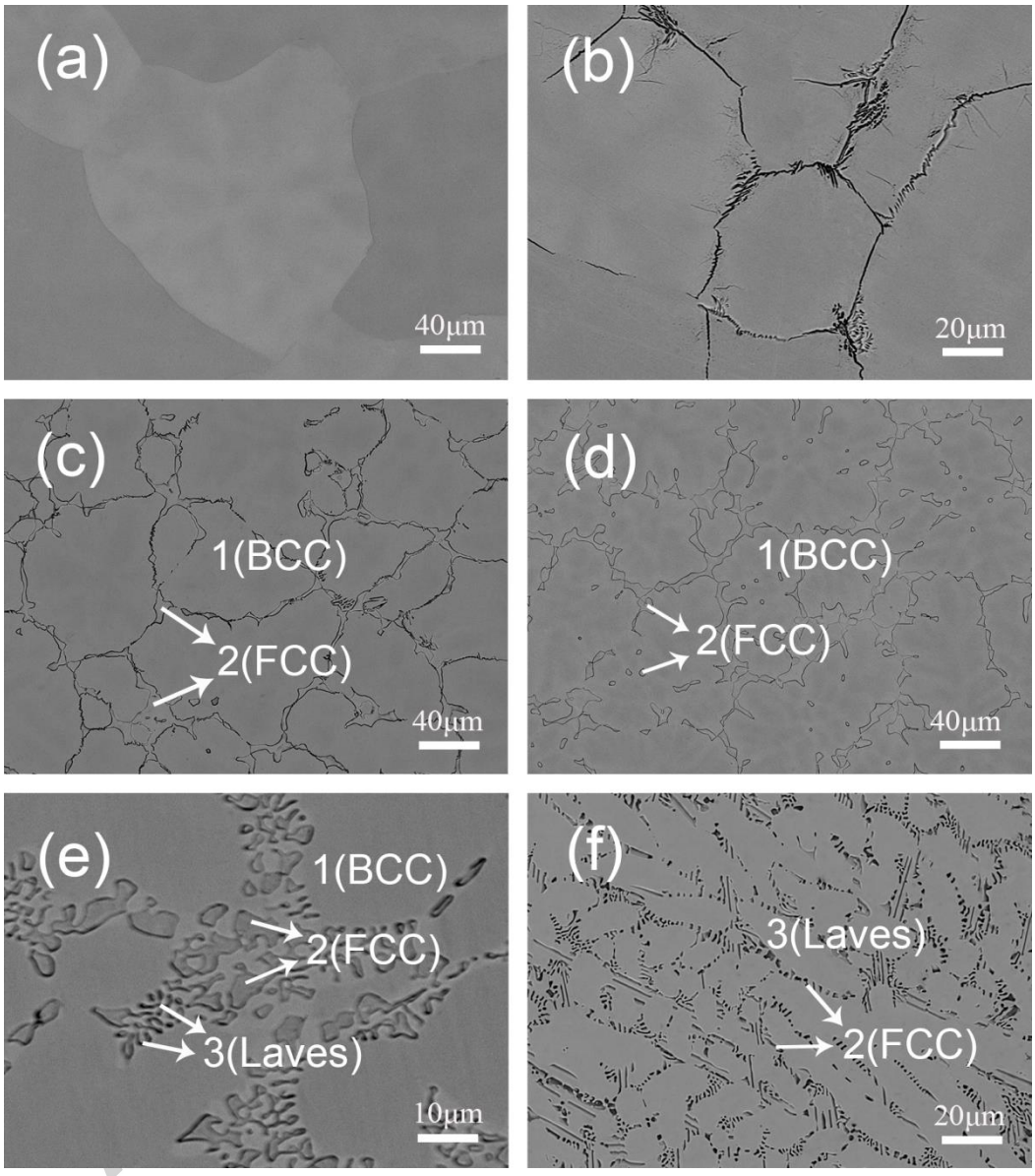

Fig. 3. Backscattered images of (a) Ti_0Al_1, (b) $Ti_{0.1}Al_{0.9}$, (c) $Ti_{0.3}Al_{0.7}$, (d) $Ti_{0.5}Al_{0.5}$, (e) $Ti_{0.8}Al_{0.2}$, and (f) Ti_1Al_0 HEAs.

Table 1

EDS analyses (at. %) of the $CoFeNiMnTi_xAl_{1-x}$ HEAs.

Alloy	Region	Co	Fe	Ni	Mn	Ti	Al
Ti_0Al_1		20.4	20.3	19.8	19.3	-	20.2
$Ti_{0.1}Al_{0.9}$		20.2	20.0	20.1	19.9	1.8	18.0
$Ti_{0.3}Al_{0.7}$	1	20.7	20.3	19.4	19.6	6.0	14.0
	2	19.9	28.5	16.9	25.7	4.1	4.9
$Ti_{0.5}Al_{0.5}$	1	20.4	20.2	19.7	19.2	9.9	10.6
	2	19.8	27.6	19.4	24.5	5.4	3.3
$Ti_{0.8}Al_{0.2}$	1	20.7	19.4	20.7	19.8	15.3	4.1
	2	18.8	28.2	19.6	24.6	8.8	-
	3	22.6	23.3	17.8	17.3	19.0	-
Ti_1Al_0	2	17.3	14.8	26.6	25.1	16.2	-
	3	22.8	22.5	15.4	16.1	23.2	-

1: BCC phase, 2: FCC phase, 3: Laves phase

Table 2

The mixing enthalpy of ΔH_{AB}^{mix}(kJ/mol) of different atom pairs in the CoFeNiMnTi$_x$Al$_{1-x}$ HEAs.

Element (Melting point, Atomic radius)	Co	Fe	Ni	Mn	Ti	Al
Co (1,495℃, 1.2510 Å)	-	-1	0	-5	-28	-19
Fe (1,538℃, 1.2412 Å)	-	-	-2	0	-17	-11
Ni (1,455℃, 1.2459 Å)	-	-	-	-8	-35	-22
Mn (1,245℃, 1.3500 Å)	-	-	-	-	-8	-19
Ti (1,668℃, 1.4615 Å)	-	-	-	-	-	-30
Al (660℃, 1.4317 Å)	-	-	-	-	-	-

3.2 Phase stability

The high mixing entropy can significantly lower the free energy, the tendency of ordering and segregation. Therefore, HEAs are more easily to form the random solid solution during solidification, rather than intermetallics or other ordered phases, especially at high temperatures [1]. However, recently, many studies indicate that the high mixing entropy is not sufficient to inhibit the formation of intermetallic phases or ordered solid solutions [27, 30]. For the purpose of assisting in analyzing the phase composition of HEAs, some phase formation criterions, based on thermodynamic parameters, are proposed and given below [1, 3, 26-33].

$$\Delta S_{mix} = -R\sum_{i=1}^{n} c_i \ln c_i \quad (1)$$

$$\delta = \sqrt{\sum_{i=1}^{n} c_i \left(1 - \frac{r_i}{\sum_{i=1}^{n} c_i r_i}\right)^2} \quad (2)$$

$$\Delta H_{mix} = \sum_{i=1, i\neq j}^{n} 4\Delta H_{AB}^{mix} c_i c_j \quad (3)$$

$$\Omega = \frac{T_m \Delta S_{mix}}{|\Delta H_m|} \quad (4)$$

$$VEC = \sum_{i=1}^{n} c_i \, (VEC)_i \quad (5)$$

$$\Delta\chi_{\text{Pauling}} = \sqrt{\sum_{i=1}^{n} c_i (\chi_i{}^{Pauling} - \chi_a)^2} \quad (6)$$

$$\Delta\chi_{\text{Allen}} = \sqrt{\sum_{i=1}^{n} c_i (1 - \chi_i{}^{Allen}/\chi_b)^2} \quad (7)$$

$$\overline{Md} = \sum_{i=1}^{n} c_i \, (Md)_i \quad (8)$$

where ΔS_{mix} is the entropy of mixing of the alloying elements [1]; c_i, R, and r_i are the mole percent of each component, gas content, and the atomic radius, respectively; δ and ΔH_{mix} are the atomic-size difference and enthalpy of mixing [3], respectively; ΔH_{AB}^{mix} is a concentration-dependent interaction parameter between elements, *i* and *j*, in a sub-regular solid-solution model [26]; Ω is a specially introduced parameter [31]; $T_m = \sum_i^n T_i$ is the average melting temperature; T_i is the melting temperature of the element, *i*; VEC is the average valence electron concentration [32]; $(VEC)_i$ is the valence electron concentration of the element, *i*; $\Delta\chi_{\text{Pauling}}$ and $\Delta\chi_{\text{Allen}}$ [33] are the Pauling- electronegativity difference and Allen electronegativity difference, respectively; $\chi_a = \sum c_i \, \chi_i{}^{Pauling}$ and $\chi_b = \sum c_i \chi_i{}^{Allen}$ are the average Pauling electronegativity and Allen electronegativity, respectively; $\chi_i{}^{Pauling}$ and $\chi_i{}^{Allen}$ are the Pauling electronegativity of the element, *i*, and Allen electronegativity of the element, *i*, respectively; $\overline{Md}$ is the average value of the d-orbital energy level [34]; and $(Md)_i$ is the d-orbital energy level of the element, *i*, in the *M*-element centered cluster in the *i*-*M* binary solid-solution alloy, in which *i* is a solvent, and *M* is a solute.

Table 3 presents the corresponding calculated parameters of δ, ΔH_{mix}, ΔS_{mix}, T_m,

VEC, $\Delta\chi_{Pauling}$, $\Delta\chi_{Allen}$, and $\overline{Md}$ for the studied $CoFeNiMnTi_xAl_{1-x}$ HEAs. The criterion of δ-Ω is generally used to predict the formation of solid-solution phases at present. It has been suggested that solid-solution phases are expected to form when $\delta < 6.6\%$ and $\Omega \geq 1.1$. In this study, the values of δ and Ω for $CoFeNiMnTi_xAl_{1-x}$ (x = 0, 0.1, 0.3, and 0.5) HEAs meet the criteria, which agree with the experimental results. It can be seen in Table 2 that the values of δ and Ω for $Ti_{0.8}Al_{0.2}$ and Ti_0Al_1 HEAs fall into the single solid-solution zone as well. However, the Laves phase appeared in the $Ti_{0.8}Al_{0.2}$ and Ti_0Al_1 HEAs. Hence, the criterion is invalid to predict the phase formation in the present HEA system. In the recent research, it was proposed that the current δ criterion did not exactly predict the formation of Laves phase [27]. The VEC also has been concluded to predict the formation of solid-solution phases [32]. All of alloys fall into the FCC + BCC region ($6.87 < VEC < 8$) on the grounds of the VEC criterion, which indicates that it is also invalid for the alloy system.

Some criteria specific to the formation of the Laves phase in HEAs have been proposed. The $\Delta\chi_{Pauling}$ parameter ($\Delta\chi_{Pauling} > 13.3$) has been used to predict the formation of the topologically-closed-packed (TCP) phase in HEAs, but it is invalid for HEAs containing too much Al [33]. The experimental results also proved the point. The $\Delta\chi_{Pauling}$ value of each alloy meets the criterion but the Laves phase was only observed in the $Ti_{0.8}Al_{0.2}$ and Ti_1Al_0 HEAs. Recently, it was proposed that Laves phase forms when $\delta > 5.0\%$ and $\Delta\chi_{Allen} > 7.0\%$ [27]. The values of δ and $\Delta\chi_{Allen}$ of the $Ti_{0.3}Al_{0.7}$ and $Ti_{0.5}Al_{0.5}$ HEAs satisfy the criterion. Nevertheless, the Laves phase vanished, which indicates the limitation of the criterion. Given the above, these

electro-negativity parameters are invalid to predict the formation of the Lave phase in the current HEA system. In addition, the average value of the d-orbital energy level ($\overline{Md} > 1.09$) was examined to predict the formation of the TCP phase as well [34]. The values of $\overline{Md}$ in Table 3 demonstrated that the $\overline{Md}$ parameter criterion predicted exactly the phase formation in the current HEA system.

Table 3

Calculated parameters of δ, ΔH_{mix}, ΔS_{mix}, T_m, Ω, VEC, $\Delta\chi_{Pauling}$, $\Delta\chi_{Allen}$, and $\overline{Md}$ for the $CoFeNiMnTi_xAl_{1-x}$ HEAs.

Alloys	δ (%)	ΔH_{mix} (kJ/mol)	ΔS_{mix} (J/mol·K)	T_m(K)	Ω	VEC	$\Delta\chi_{Pauling}$ (%)	$\Delta\chi_{Allen}$ (%)	$\overline{Md}$ (eV)
Ti_0Al_1	5.80	-13.92	13.38	1,278.20	1.23	7.40	14.72	5.20	1.042
$Ti_{0.1}Al_{0.9}$	5.88	-14.62	13.92	1,298.36	1.24	7.42	14.89	5.96	1.049
$Ti_{0.3}Al_{0.7}$	6.04	-15.74	14.40	1,338.68	1.22	7.46	15.22	7.22	1.056
$Ti_{0.5}Al_{0.5}$	6.19	-16.48	14.53	1,379.00	1.21	7.50	15.54	8.28	1.079
$Ti_{0.8}Al_{0.2}$	6.41	-16.86	14.21	1,439.48	1.24	7.56	16.00	9.20	1.101
Ti_1Al_0	6.56	-16.64	13.38	1,479.80	1.19	7.60	16.29	10.42	1.116

3.3 Mechanical properties

The room-temperature compressive stress-strain curves are shown in Fig 4. The yield strength (σ_y), compressive strength (σ_{max}), and fracture strain (ε_f) are presented in Table 4. The Ti_0Al_1 HEA has poor strength and ductility. As the Ti with larger atomic radius dissolves in the BCC solid solution structure and occupies the lattice sites, the lattice distortion energy increases significantly so that the effect of solid-solution

strengthening is enhanced. Compared with the Ti_0Al_1 HEA, the yield strength and the fracture strength of the $Ti_{0.1}Al_{0.9}$ HEA increase. With the increase of the Ti content and the decrease of the Al content, the structure changes from BCC to BCC + FCC phases. The ductility of the alloys markedly improves. The volume fractions of the FCC phase in the $Ti_{0.3}Al_{0.7}$ and $Ti_{0.5}Al_{0.5}$ HEAs are 10.2% and 13.7%, respectively. However, for the $Ti_{0.8}Al_{0.2}$ HEA, the formation of the Laves phase benefits the strength with sacrificing the compressive ductility. The Ti_1Al_0 HEA has poor ductility because the hard Laves phase becomes the primary phase. In conclusion, the $Ti_{0.5}Al_{0.5}$ HEA has a balanced yield strength (1,052.8 MPa), fracture strength (2,402.4 MPa) and fracture strain (20.5%).

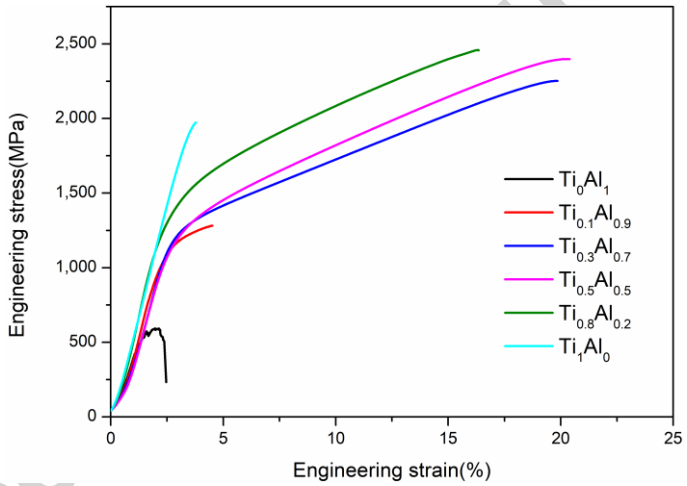

Fig. 4. Compressive stress-strain curves for the $CoFeNiMnTi_xAl_{1-x}$ HEAs.

Table 4

Compression yield stress (σ_y), fracture strength (σ_{max}), and fracture strain (ε_p) of the $CoFeNiMnTi_xAl_{1-x}$ HEAs

Alloy	σ_y (MPa)	σ_{max} (MPa)	ε_p (%)
Ti_0Al_1	577.4	602.3	1.9
$Ti_{0.1}Al_{0.9}$	926.7	1,129.3	16.2
$Ti_{0.3}Al_{0.7}$	1,106.6	2,252.1	19.3
$Ti_{0.5}Al_{0.5}$	1,052.8	2,402.4	20.5
$Ti_{0.8}Al_{0.2}$	1,125.8	2,464.5	16.3
Ti_1Al_0	1,070.5	1,972.8	3.8

Hardness is a significant mechanical performance index as well. The Vickers hardness values of the $CoFeNiMnTi_xAl_{1-x}$ HEAs are given in Fig 5. The hardness values of the $CoFeNiMnTi_xAl_{1-x}$ (x = 0, 0.1, 0.3, 0.5, 0.8, and 1) HEAs are HV455.2, HV525.5, HV520.1, HV518.7, HV530.6, and HV708.4, respectively. All alloys exhibit high hardness due to the fact that the main phase is the BCC structure for the Ti_xAl_{1-x} (x = 0, 0.1, 0.3, 0.5, and 0.8) HEAs, and the main phase is the Laves phase for the Ti_1Al_0 HEA. Both the BCC phase and the Laves phase are hard. It is clearly seen that compared with the Ti_0Al_1 HEA, hardness of the $Ti_{0.1}Al_{0.9}$ HEA improves due to the strong effect of solid-solution hardening. Ti can increase the bonding strength and then increase the hardness [35]. Compared with the $Ti_{0.1}Al_{0.9}$ HEA, the hardness values of the $Ti_{0.3}Al_{0.7}$ and $Ti_{0.5}Al_{0.5}$ HEAs decrease slightly. Depending on the XRD and SEM analyses, this trend is caused by the increase in the volume fraction of the FCC phase. The increase of the hardness value of the $Ti_{0.8}Al_{0.2}$ HEA is attributed to the formation

of a few hard Laves phases. Furthermore, the hardness value of the Ti_1Al_0 HEA increases markedly because the Laves phase becomes the primary phase.

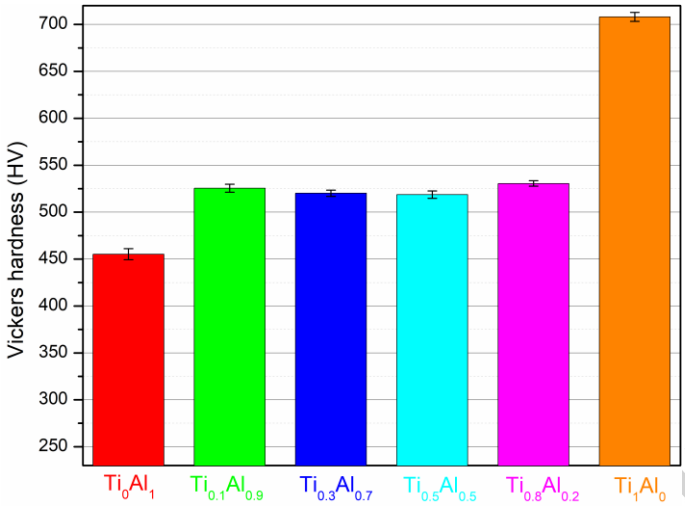

Fig. 5. Hardness of $CoFeNiMnTi_xAl_{1-x}$ HEAs.

In order to further verify the fundamental mechanism of the ductility variation in the $CoFeNiMnTi_xAl_{1-x}$ HEAs, fracture surfaces after compressive tests were examined. Figure 6 shows the SEM images of the compression fracture morphologies. The fracture morphologies of the Ti_0Al_1, $Ti_{0.1}Al_{0.9}$, and Ti_1Al_0 HEAs exhibit typical cleavage fracture features. Petal-like or river-like patterns and cleavage steps can be observed from the fracture surfaces. Nevertheless, obvious torn edges and dimples-like structures were found on the fracture surface of the other alloys, which indicates that the alloys have higher ductility. The characteristics of the fracture surfaces agree with the compression and hardness tests.

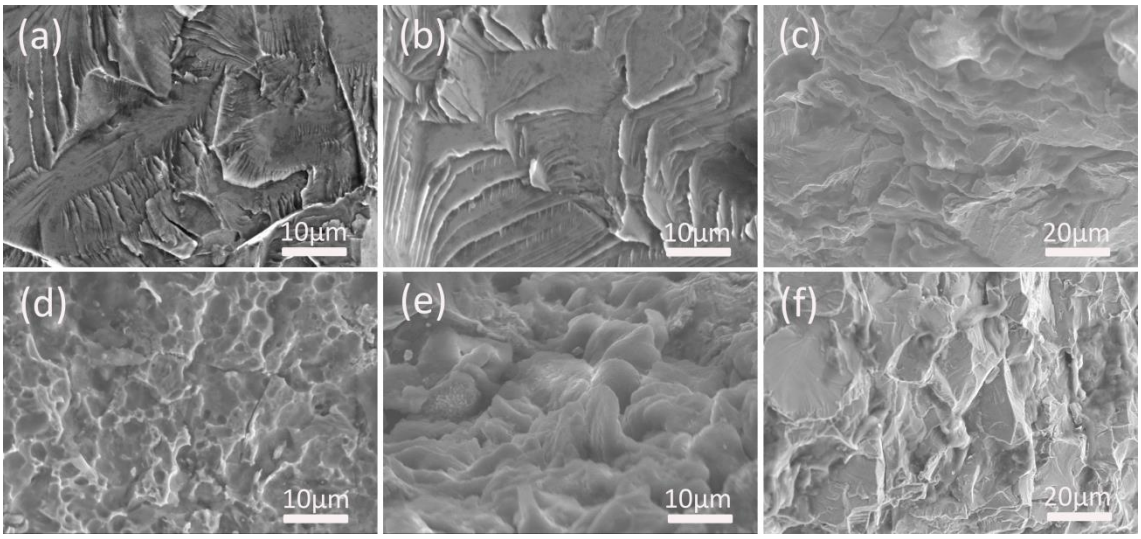

Fig.6. Fracture SEM images of (a) Ti_0Al_1, (b) $Ti_{0.1}Al_{0.9}$, (c) $Ti_{0.3}Al_{0.7}$, (d) $Ti_{0.5}Al_{0.5}$, (e) $Ti_{0.8}Al_{0.2}$, and (f) Ti_1Al_0 HEAs.

3.4 Nanoindention

The dual-phase (BCC + FCC) $Ti_{0.5}Al_{0.5}$ HEA has the optimal performance of both strength and ductility, and was further investigated by nanoindentation experiments. The load-depth curves of different phases are shown in Fig. 7(a). The values of the maximum penetration depth in the FCC and BCC phases are 158.3 nm and 241.2 nm, respectively. It can be clearly seen that the indentation in the FCC phase is greater than that in the BCC phase under the same load. According to the Oliver-Pharr method [36], Fig. 7(b) presents the nanohardness data and elastic modulus values of the different phases. The average nanohardness of the BCC phase (7.7 GPa) is more than two times of the FCC phase (3.2 GPa). The elastic modulus values of the FCC and BCC phases are 189.3 GPa and 196.9 GPa, respectively. The values of nanohardness and elastic modulus of the BCC matrix are higher, which directly indicates that the BCC matrix has higher strength and hardness than the FCC phase.

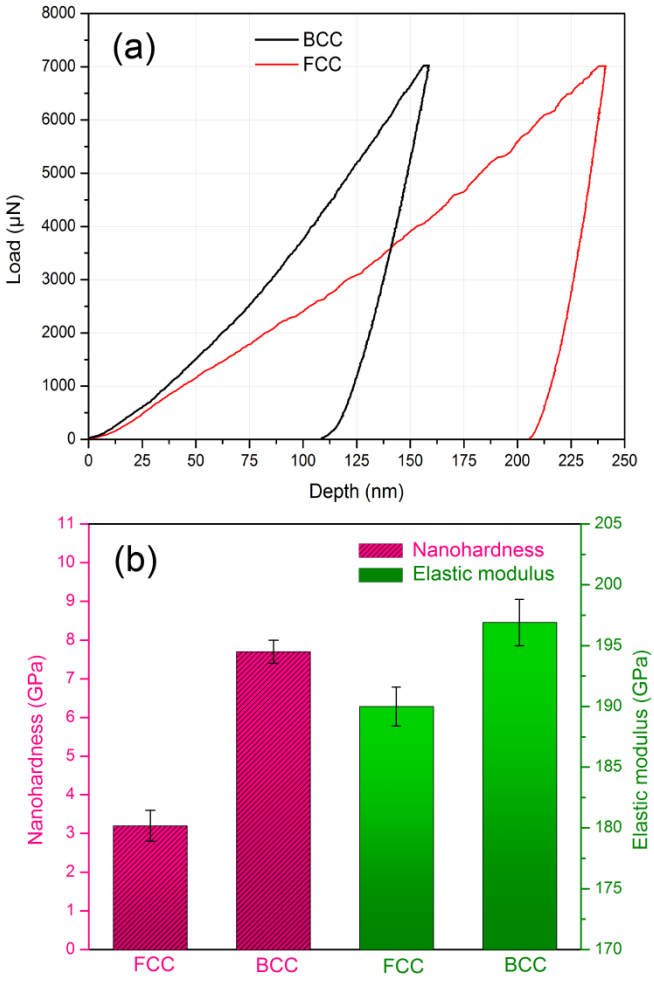

Fig. 7. (a) Typical load-displacement (*P*-*h*) curves for nanoindentation within the BCC matrix and FCC phase of the $Ti_{0.5}Al_{0.5}$ HEA. (b) The average nanohardness and elastic modulus on different phases of the $Ti_{0.5}Al_{0.5}$ HEA.

The incipient plasticity can be marked by a sudden displacement burst (or pop-in) in the measured load-displacement curve. The first pop-in behavior represents the elastic-to-plastic transition [37-39]. Before the first pop-in, the deformation is elastic. Based on the Hertzian contact theory [38], the elastic behavior follows the relationship:

$$P = \frac{4}{3} E_r R^{1/2} h^{3/2} \quad (9)$$

where P is the intendation load, R is the tip radius, h is indentation depth, and E_r is the

reduced modulus, calculated by

$$\frac{1}{E_r} = \frac{1-{v_1}^2}{E_1} + \frac{1-{v_2}^2}{E_2} \quad (10)$$

where E_i (= 1,141GPa) and v_i (= 0 .07) are the Young's modulus and Poisson's ratio of the diamond indenter, and E_s, and v_s are the Young's modulus and Poisson's ratio of the sample, respectively. The elastic portion of the loading curves was well fitted by Eq.(9), as shown in Fig. 8(a). The average values of the reduced modulus are shown in Fig. 8(b).

According to the continuum mechanics, the maximum shear stress, τ_{max}, is located directly beneath the bottom of the contact at a depth of 0.48 times the contact radius [40]. The value of τ_{max} can be given using the follow equation：

$$\tau_{max} = 0.31p_0 = 0.31\left(\frac{3}{2}p_m\right) = 0.31(\frac{6{E_r}^2}{\pi^3 R^2}\mathrm{P})^{\frac{1}{3}} \quad (11)$$

where p_0 and p_m are the maximum and mean pressures of the contact at the pop-in, respectively. The pop-in stress is generally in the range of 1/30G – 1/5G, where G is the shear modulus, corresponding to the theoretical strength of the crystal [22]. As shown in Fig. 8(b), τ_{max} of the FCC phase was calculated as 3.1 GPa, which corresponds to $1/22G_{FCC}$, where G_{FCC} is the shear modulus of the FCC phase (~ 72.8 GPa, estimated from the Young's modulus and a Poisson's ratio of 0.3). The τ_{max} of the BCC phase was calculated as 4.5 GPa ($1/17\ G_{BCC}$), where G_{BCC} (~ 75.7 GPa) is the shear modulus of the BCC phase. The τ_{max} of the BCC phase is higher than that of the FCC phase. The higher contents of Ti and Al with large atomic radii in the BCC matrix cause more severe lattice distortion and result in the higher activation energy of dislocation nucleation of the BCC matrix. High activation energy would make

dislocation nucleation more difficult. Ye *et al.* found that the activation energy for pop-ins in the BCC-HEA is higher than that in the FCC-HEA, and proposed that the nucleation of the full dislocation is favored in the BCC-HEA while the nucleation of the partial dislocation is favored in FCC-HEA [23].

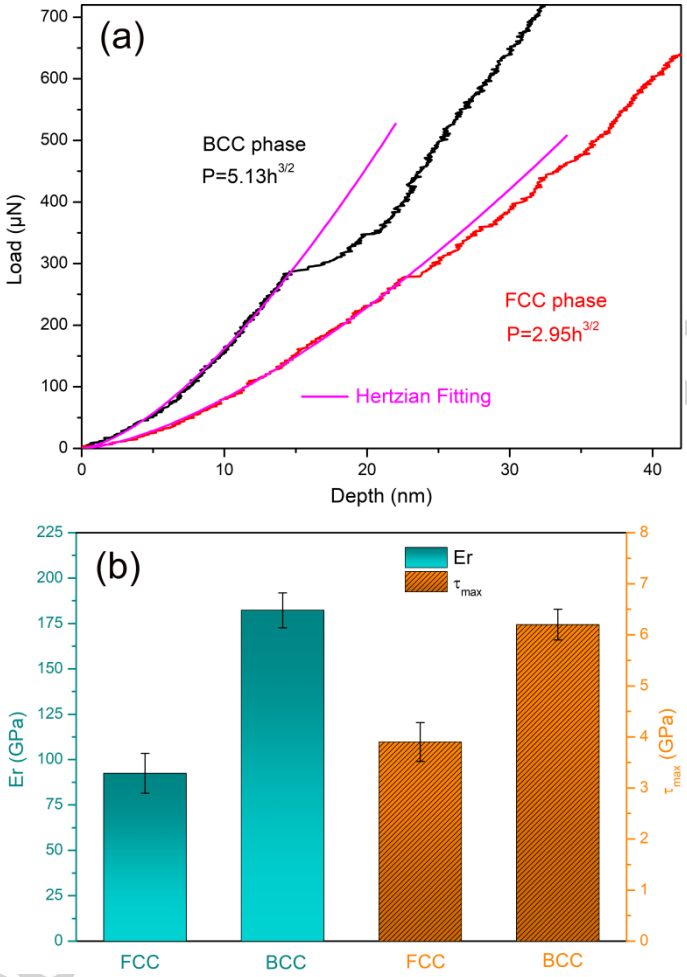

Fig. 8. (a) A typical first pop-in event at the beginning of the *P-h* curves of the BCC matrix and FCC phase obtained with nanoindentation. (b) Average reduced modulus and the maximum shear stress on the BCC matrix and FCC phase of the $Ti_{0.5}Al_{0.5}$ HEA.

4. Conclusions

In this study, effects of the addition of various amounts of Al and Ti on the microstructure and mechanical properties of $CoFeNiMnTi_xAl_{1-x}$ (x = 0, 0.1, 0.3, 0.5,

0.8, and 1) HEAs were investigated and the following conclusions were drawn.

(1) With the increase of the Ti content and the decrease of the Al content, the crystal structure changes from BCC to BCC + FCC to BCC + FCC + Laves and then to Laves + FCC phases in the $CoFeNiMnTi_xAl_{1-x}$ HEAs.

(2) The criteria ($\Omega - \delta$, *VEC*, $\Delta\chi_{Pauling}$, and $\Delta\chi_{Allen}$) are invalid to predict the phase formation of the $CoFeNiMnTi_xAl_{1-x}$ HEAs. The criterion ($\overline{Md} > 1.09$) is more suitable for predicting the formation of the Laves phase in the current alloy system.

(3) The two-phase (BCC + FCC) $CoFeNiMnTi_{0.5}Al_{0.5}$ HEA has a balance of strength and ductility. The yield strength, fracture strength, and strain can reach 1,052.8 MPa, 2,402.4 MPa, and 20.5%, respectively. The hardness reaches HV518.7.

(4) The BCC matrix and FCC phase in the $CoFeNiMnTi_{0.5}Al_{0.5}$ HEA were studied by nanoindentation technique. The nanohardness and elastic modulus of the BCC matrix phase are 7.7 GPa and 196.9 GPa, and the nanohardness and elastic modulus of the FCC phase are 3.2 GPa and 189.3 GPa, respectively. Moreover, the maximum shear stress of the BCC matrix phase (4.5 GPa) is higher than that of the FCC phase (3.1 GPa), and the dislocation nucleation of the BCC phase is more difficult.

Acknowledgments

This work was supported by the National Science Foundation of China (Grant No. 11674274), the Basic Research Project in the Hebei Province (Grant No. A2016203382), the Research Program of the College Science & Technology of the

Hebei Province (Grant No. QN2016167), and the National Natural Science Funds of China (Grant No. 51601166).

References

[1] J. Yeh, S. Chen, S. Lin, J. Gan, T. Chin, T. Shun, C. Tsau, S. Chang, Advanced Engineering Materials, 6 (2004) 299-303.

[2] Y. Zhang, T.T. Zuo, Z. Tang, M.C. Gao, K.A. Dahmen, P.K. Liaw, Z.P. Lu, Progress in Materials Science, 61 (2014) 1-93.

[3] Y. Zhang, Y.J. Zhou, J.P. Lin, G.L. Chen, P.K. Liaw, Advanced Engineering Materials, 10 (2008) 534-538.

[4] D. Li, C. Li, T. Feng, Y. Zhang, G. Sha, J.J. Lewandowski, P.K. Liaw, Y. Zhang, Acta Materialia, 123 (2017) 285-294.

[5] Y. Shi, B. Yang, X. Xie, J. Brechtl, K.A. Dahmen, P.K. Liaw, Corrosion Science, 119 (2017) 33-45.

[6] B. Gludovatz, A. Hohenwarter, D. Catoor, E.H. Chang, E.P. George, R.O. Ritchie, Science, 345 (2014) 1153-1158.

[7] D. Liu, P. Yu, G. Li, P.K. Liaw, R. Liu, Materials Science and Engineering: A, 724 (2018) 283-288.

[8] Y. Wu, W.H. Liu, X.L. Wang, D. Ma, A.D. Stoica, T.G. Nieh, Z.B. He, Z.P. Lu, Applied Physics Letters, 104 (2014) 633-693.

[9] W.H. Liu, Z.P. Lu, J.Y. He, J.H. Luan, Z.J. Wang, B. Liu, Y. Liu, M.W. Chen, C.T. Liu, Acta Materialia, 116 (2016) 332-342.

[10] L.J. Zhang, P.F. Yu, M.D. Zhang, D.J. Liu, Z. Zhou, M.Z. Ma, P.K. Liaw, G. Li, R.P. Liu, Materials Science and Engineering: A, 707 (2017) 708-716.

[11] P.F. Yu, H. Cheng, L.J. Zhang, H. Zhang, Q. Jing, M.Z. Ma, P.K. Liaw, G. Li, R.P. Liu, Materials Science and Engineering: A, 655 (2016) 283-291.

[12] B. Wu, Z. Xie, J. Huang, J. Lin, Y. Yang, L. Jiang, J. Huang, G. Ye, C. Zhao, S. Yang, B. Sa, Intermetallics, 93 (2018) 40-46.

[13] A. Munitz, M.J. Kaufman, M. Nahmany, N. Derimow, R. Abbaschian, Materials Science and Engineering: A, 714 (2018) 146-159.

[14] T. Yang, S. Xia, S. Liu, C. Wang, S. Liu, Y. Zhang, J. Xue, S. Yan, Y. Wang, Materials Science and Engineering: A, 648 (2015) 15-22.

[15] C.J. Tong, Y.L. Chen, J.W. Yeh, S.J. Lin, S.K. Chen, T.T. Shun, C.H. Tsau, S.Y. Chang, Metallurgical & Materials Transactions A, 36 (2005) 881-893.

[16] B. Wu, W. Chen, Z. Jiang, Z. Chen, Z. Fu, Materials Science and Engineering: A, 676 (2016) 492-500.

[17] Z. Wang, M. Wu, Z. Cai, S. Chen, I. Baker, Intermetallics, 75 (2016) 79-87.

[18] M.-H. Chuang, M.-H. Tsai, W.-R. Wang, S.-J. Lin, J.-W. Yeh, Acta Materialia, 59 (2011) 6308-6317.

[19] Z. Wu, H. Bei, F. Otto, G.M. Pharr, E.P. George, Intermetallics, 46 (2014) 131-140.

[20] T. Zuo, M.C. Gao, L. Ouyang, X. Yang, Y. Cheng, R. Feng, S. Chen, P.K. Liaw, J.A. Hawk, Y. Zhang, Acta Materialia, 130 (2017) 10-18.

[21] V. Maier-Kiener, B. Schuh, E.P. George, H. Clemens, A. Hohenwarter, Materials & Design, 115 (2017) 479-485.

[22] C. Zhu, Z.P. Lu, T.G. Nieh, Acta Materialia, 61 (2013) 2993-3001.

[23] Y.X. Ye, Z.P. Lu, T.G. Nieh, Scripta Materialia, 130 (2017) 64-68.

[24] Y.J. Zhou, Y. Zhang, Y.L. Wang, G.L. Chen, Applied Physics Letters, 90 (2007) 181904.

[25] X.F. Wang, Y. Zhang, Y. Qiao, G.L. Chen, Intermetallics, 15 (2007) 357-362.

[26] A. Takeuchi, A. Inoue, Materials Transactions, 46 (2005) 2817-2829.

[27] N. Yurchenko, N. Stepanov, G. Salishchev, Materials Science and Technology, 33 (2016) 17-22.
[28] F. He, Z. Wang, P. Cheng, Q. Wang, J. Li, Y. Dang, J. Wang, C.T. Liu, Journal of Alloys and Compounds, 656 (2016) 284-289.
[29] N.D. Stepanov, N.Y. Yurchenko, V.S. Sokolovsky, M.A. Tikhonovsky, G.A. Salishchev, Materials Letters, 161 (2015) 136-139.
[30] N.D. Stepanov, D.G. Shaysultanov, G.A. Salishchev, M.A. Tikhonovsky, E.E. Oleynik, A.S. Tortika, O.N. Senkov, Journal of Alloys and Compounds, 628 (2015) 170-185.
[31] X. Yang, Y. Zhang, Materials Chemistry and Physics, 132 (2012) 233-238.
[32] S. Guo, C. Ng, J. Lu, C.T. Liu, Journal of Applied Physics, 109 (2011) 213.
[33] Y. Dong, Y. Lu, L. Jiang, T. Wang, T. Li, Intermetallics, 52 (2014) 105-109.
[34] Y. Lu, Y. Dong, L. Jiang, T. Wang, T. Li, Y. Zhang, Entropy, 17 (2015) 2355-2366.
[35] T.-T. Shun, L.-Y. Chang, M.-H. Shiu, Materials Science and Engineering: A, 556 (2012) 170-174.
[36] W.C. Oliver, G.M. Pharr, Journal of Materials Research, 7 (1992) 1564-1583.
[37] J.R. Morris, H. Bei, G.M. Pharr, E.P. George, Physical Review Letters, 106 (2011) 165502.
[38] F.F.G. G., Nature, 55 (1896) 6-9.
[39] W. Wang, C.B. Jiang, K. Lu, Acta Materialia, 51 (2003) 6169-6180.
[40] J.K. Mason, A.C. Lund, C.A. Schuh, Physical Review B, 73 (2006) 054102.